J Mater Sci: Mater Electron (2015) 26:2614–2621
DOI 10.1007/s10854-015-2732-x

Sol–gel synthesis, structural, optical and magnetic properties of Co-doped ZnO nanoparticles

J. El Ghoul · M. Kraini · O. M. Lemine · L. El Mir

Received: 27 November 2014 / Accepted: 19 January 2015 / Published online: 30 January 2015

Abstract We report the synthesis of $Zn_{1-x}Co_xO$ nanoparticles prepared by a sol–gel processing technique for x ranging from 0 to 0.05. The structural, morphological, optical and magnetic properties of the as-prepared nanoparticles were investigated by XRD, XPS, transmission electron microscopy, UV measurements, photoluminescence and superconducting quantum interference device. The structural properties showed that the obtained nanoparticles are single phase wurtzite structure and no secondary phases were detected which indicated that Co ions substituted for Zn ions. The energy gap decreased gradually with increasing doping concentration of Co. The photoluminescence spectra show a shift of the position of the ultraviolet emission to long wavelength and the intensity decreases with increasing Co. The Magnetic measurements at room temperature reveal diamagnetic behavior for sample with lower concentration and the presence of both paramagnetic and ferromagnetic behavior for increasing concentration.

1 Introduction

In recent years, semiconductor nanoparticles have attracted great interest [1–3]. This is stimulated mainly by physical probe into low-dimensional systems and potential applications for this class of materials. They always exhibit novel optical, electrical, and mechanical properties due to quantum confinement effects compared with their bulk counterparts, and thus can be applied in many areas, including luminescent devices, solar cells, chemical sensors, and biological labeling and diagnostics.

Due to its excellent optical, electrical, mechanical and chemical properties, ZnO semiconductor has attracted a great deal of attention in the material research field. Due to its significant optical and electronic properties, ZnO has been widely used for fabricating various nano-optoelectronic devices [4–7]. Recently, the doping of well-chosen impurities has been extensively explored as an effective technique to modify the properties of ZnO nanostructures [8–12]. Transition metal doping of ZnO has become an active research field ever since it was predicted to improve the optical and electronic properties of the oxide material, and particularly, lead to room-temperature ferromagnetism. Among these, the element of Co is considered a potential candidate for incorporating into ZnO because of its abundant electron states and large solubility in the ZnO matrix [13]. Many groups have synthesized Co-doped ZnO nanostructures and studied the altered performance upon doping. For instance, Jones and coworkers [14] fabricated Co:ZnO submicrometer tubes using a polymer based template approach. They observed a 25-nm redshift in UV–vis absorption, which originated from the narrowing of the ZnO band gap (3.22 eV) as a result of Co doping. Wang et al. [15] synthesized Co:ZnO nanorod arrays on a glass substrate via a solution route. They found that Co doping can effectively adjust the energy level in ZnO nanorods, lead to variation in the UV emission peak position, and enhance the luminescence performance in the visible light region. Bahadur et al. [16] synthesized

J. El Ghoul · M. Kraini · L. El Mir
Laboratory of Physics of Materials and Nanomaterials Applied at Environment (LaPhyMNE), Faculty of Sciences in Gabes, Gabes University, 6072 Gabès, Tunisia

J. El Ghoul · O. M. Lemine (✉) · L. El Mir
Department of Physics, College of Sciences, Al Imam Mohammad Ibn Saud Islamic University (IMISU), Riyadh 11623, Saudi Arabia
e-mail: leminej@yahoo.com

uniform and transparent $Zn_{1-x}Co_xO$ films by a sol–gel spin coating technique, and revealed that an increase in Co content in the range $0 \leq x \leq 0.10$ led to a decrease in band gap energy as well as quenching of the near band edge and blue emissions. Sharma et al. [17] prepared Co:ZnO nanoparticles by a co-precipitation technique. The obtained samples showed strong ferromagnetic behavior at room temperature. However, at higher doping levels, the ferromagnetic behavior was suppressed and the antiferromagnetic nature was enhanced. Xu and Cao [18] reported a hydrothermal method to synthesize $Zn_{1-x}Co_xO$ flakes, and found that the samples exhibited obvious ferromagnetic characteristics at room temperature. Moreover, with more doping content of Co^{2+}, the ferromagnetic behavior was suppressed and paramagnetic nature was observed. Previous studies have obviously demonstrated that the physical and chemical properties of the synthesized $Zn_{1-x}Co_xO$ samples are strongly sensitive to its preparative conditions [15, 16]. Over the past few years, much effort has been made to investigate wet chemical methods for the synthesis of metal-ion-doped ZnO nanostructures, including the sol–gel method [19, 20] and various hydrothermal methods [21, 22]. Motivated by these reasons, we report in this paper a new approach to obtain such powders based on hydrolysis of zinc acetate in methanol followed by supercritical drying in ethanol using modified sol–gel process. The effect of cobalt as transition metal (TM) doping element on structural, optical and magnetic properties of the powder is investigated for different concentrations.

2 Experimental

Cobalt-doped ZnO nanocrystals were prepared by the sol–gel method using 16 g of zinc acetate dehydrate as precursor in a 112 ml of methanol. After magnetic stirring at room temperature, the appropriate amount of cobalt acetate was added, and the solution was placed in an autoclave and dried under supercritical conditions of ethyl alcohol.

X-ray diffraction (XRD) patterns of cobalt doped zinc oxide nanopowder were carried out by a Bruker D5005 diffractometer, using CuKα radiation (λ = 1.5418 Å).

Crystallite sizes (G, in Å) were estimated from the Debye–Sherrer equation [23]:

$$G = {}^{0.9\lambda}/_{B\cos\theta_B} \quad (1)$$

where λ is the X-ray wavelength (1. 5418 Å), θ_B is the maximum of the Bragg diffraction peak and B is the linewidth at half maximum. The dopant content and the chemical bonding states of cobalt ions in the $Zn_{1-x}Co_xO$ nanocrystallites were determined using XPS(PHI-5702).

The synthesized products were also characterized using a JEM-200CX transmission electron microscopy (TEM). The specimens for TEM were prepared by putting the as-grown products in EtOH and immersing them in an ultrasonic bath for 15 min, then dropping a few drops of the resulting suspension containing the synthesized materials onto TEM grid. Room-temperature optical spectra in the wavelength range from 200 to 2,000 nm were collected using a Schimadzu UV-3101 PC spectrophotometer fitted with an integrating sphere diffuse reflectance accessory. The spectrophotometer measures reflectance relative to a background scatterer, which was powdered $BaSO_4$. For photoluminescence (PL) measurements, the 337.1 nm laser line of a Laser Photonics LN 100 nitrogen laser was used as an excitation source. The emitted light from the sample, collected by an optical fiber on the same side as the excitation, was analyzed with a Jobin-Yvon Spectrometer HR460 and a multichannel CCD detector (2,000 pixels). Magnetic measurements were carried out as a function of temperature (2–400 K) and magnetic field (0 to ± 60 kOe) using a commercial superconducting quantum interference device (SQUID) magnetometer (Quantum Design, MPMS XL).

3 Results and discussion

Figure 1 shows the XRD patterns of $Zn_{1-x}Co_xO$ ($0.0 \leq x \leq 0.05$) samples, which were indexed using POWDER-X software as the ZnO wurtzite structure and well matched with the standard data (JCPDS, 36-1451). It can be clearly seen from the XRD patterns that all the samples showed a single phase nature with hexagonal wurtzite structure [23]. No secondary phase was detected and this indicates that the

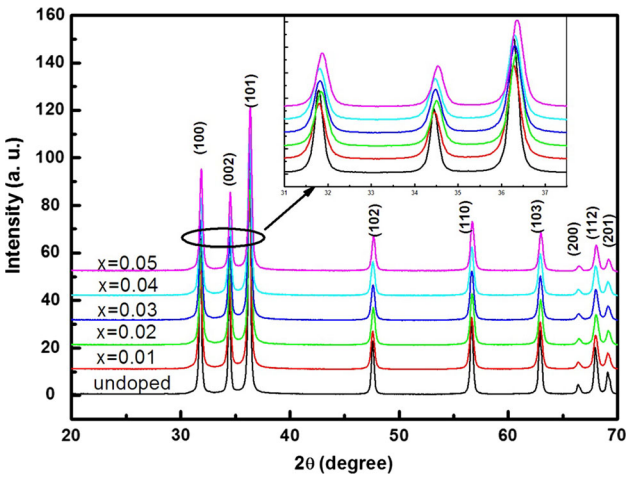

Fig. 1 XRD patterns of $Zn_{1-x}Co_xO$ nanoparticles. The *inset* displays the shifting and broadening of (100), (002) and (101) peaks for increasing Co content

Co dopant is incorporated into the lattice as a substitutional atom. We can notice also that the peaks are very broad which indicates the formation of very fine particles in the nanoscale range. The average crystallite size obtained using Debye–Scherer formula confirmed this result. Table 1 summarizes the lattices parameters obtained for several concentrations. It can be seen that the lattice parameter c values of $Zn_{1-x}Co_xO$ are smaller than the value of undoped ZnO (c = 5.208), which is close to the standard value [ICSD reference number: 67,848–1,993 (5.2121 Å) and 67,454–1,989 (5.2071 Å)]. Figure 2 shows the evolution of the lattice parameters c calculated from the XRD for different concentrations. We observed a decrease in the lattice constant value with increasing concentration of Co ions. This decrease of lattice constant with Co contents is corroborated by the shift of the peaks position (inset in Fig. 1), which generally indicates a decrease in the lattice parameters. Moreover, with increasing the Co doping content, we also found that the intensity of the diffraction peak decreased gradually and the width broadened, which might be due to the increase in the lattice disorder and strain induced by Co^{2+} substitution. The decrease of lattice can be explained by the fact that effective ionic radius of Co^{2+} (0.58 Å) in tetrahedral configuration is smaller than that of Zn^{2+} (0.60 Å) ions [24]. This reduction in lattice parameter may also be due to a diminution in size of the nanoparticles after doping [25]. In addition, for x = 0.05, we observed an increase of the lattice parameters which can be explained by the incorporation of Co^{3+} ions with significant lattice defects [26].

The average grain size was calculated from Scherer's formula (1) using the most intense peak (101) and the values are summarizes in Table 1. As shown in Fig. 2, the grain size decreases with increasing concentration of Co.

To confirm further the chemical bonding states of Co ions in the doped ZnO, XPS measurements were carried out on the samples. Figure 3a presents the full-spectrum of the $Zn_{1-x}Co_xO$ (x = 0.05) sample. The selected data has been corrected with C1s (287.2 eV). Only the characteristic peaks of Zn, O and Co are observed in the spectrum. Figure 3b and c presents the high-resolution scan of O1s and Co 2p. From the scan, the binding energies of O1s, $Co2p_{3/2}$ and $Co2p_{1/2}$ are identified as 531.1, 780.9 and 796.8 eV, respectively. There are two main peaks shown in Fig. 3d, positioned at the binding energy sites of 1,019.7 and 796.9 eV, corresponding to the $Zn2p_{3/2}$ and $Zn2p_{1/2}$ orbitals, respectively. We note that the energy difference of 15.9 eV between $Co2p_{1/2}$ and $Co2p_{3/2}$ accords with the data in the published literature on Co2p in Co–O and Co:ZnO [27, 28], which confirms the 2p oxidation state of the incorporated dopant. Therefore, Co clusters can be ruled out in the doped samples. Thus, Co ions, in the 2+ oxidation state, are surrounded by O ions, that is, Co^{2+} successfully substitute for Zn^{2+} in the ZnO lattice.

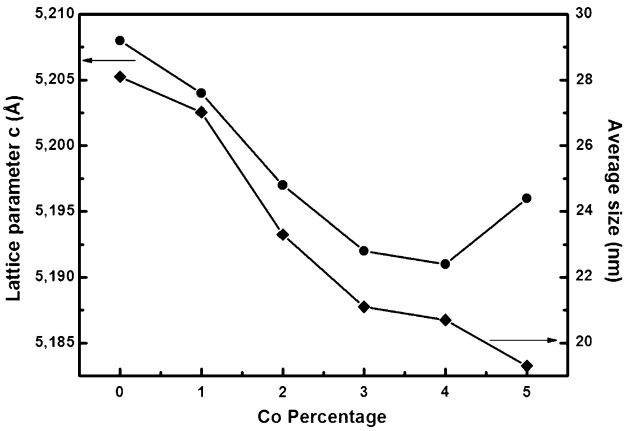

Fig. 2 Co doping concentration dependency of the lattice constant c and average size of $Zn_{1-x}Co_xO$ nanoparticles calculated using the XRD peaks

Figure 4a–d shows the TEM images for samples $Zn_{1-x}Co_xO$ with different concentration (x = 0.0, 0.01, 0.03 and 0.05). It can be seen that the samples are nearly spherical with the diameters ranging from 18 to 30 nm. It can also be noticed from these images that the average particle decreases with increasing concentration of Co, which is in agreement with XRD results. HRTEM image (Fig. 4e) showed that the measured distance between the planes is around 0.260 nm, which is corresponding to the (002) planes of the wurtzite ZnO. The EDX spectra of the doped samples are shown in Fig. 4g, h. Zn and O appeared as the main components with low levels of Co. An increase in the relative intensities of the Co peaks with increasing concentration was also observed, confirming the

Table 1 Co doping concentration dependency of the average size, lattice constant c and band gap energies of $Zn_{1-x}Co_xO$ nanoparticles

Concentration of Co (%)	Average size (nm)	Lattice parameter c (Å)	Energie (eV)
0	28,1	5,208	3,335
1	27,02	5,204	3,135
2	23,3	5,197	3,087
3	21,1	5,192	3,021
4	20,7	5,191	2,993
5	19,3	5,196	2,972

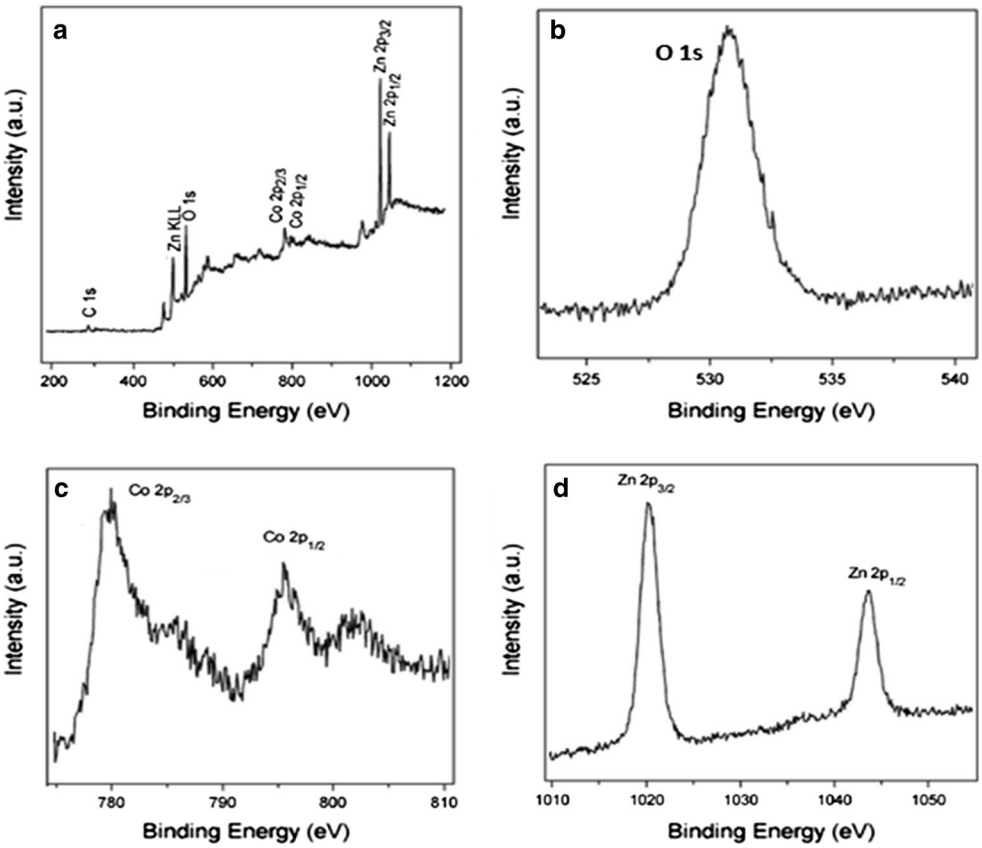

Fig. 3 XPS spectrum of $Zn_{0.95}Co_{0.05}O$ nanoparticles

progressive incorporation of Co. This ensures the uniform distribution of the doped Co ions as expected in the chemical synthesis process employed in this work.

Optical diffuse reflectance spectra of undoped and doped ZnO nanorods, measured at room temperature, are shown in Fig. 5. In the case of Co-doped nanorods, three extra absorption bands have been observed at 655, 615 and 565 nm. Based on the optical studies performed of Co-doped ZnO single crystals [29], these edges are assigned to the d–d crystal-field transitions $^4A_2(F) \rightarrow {}^2E(G)$, $^4A_2(F) \rightarrow {}^4T_1(P)$ and $^4A_2(F) \rightarrow {}^2T_1(G)$. The appearance of these transitions clearly suggests that the doped Co^{2+} is in the high-spin (S = 3/2) state and are under a tetrahedral crystal field, in agreement with similar studies on $Zn_{1-x}Co_xO$ thin films [30]. Wurtzite ZnO has Zn^{2+} ions in tetrahedral sites [31] and therefore Co^{2+} ions seem to substitute for the Zn^{2+} ions in the ZnO lattice.

The reflectance spectral data were converted to the Kubelka–Munk function, F(R) by applying the equation:

$$F(R) = \frac{(1-R)^2}{2R} \quad (2)$$

The direct band gap (Eg) energies of the $Zn_{1-x}Co_xO$ powders were calculated from their diffuse–reflectance spectra by plotting $[F(R)\cdot h\nu]^n$ versus $h\nu$. A direct band gap semiconductor gives a linear Tauc region just above the optical absorption edge with n = 2, whilst an indirect semiconductor gives a linear region with n = 0.5 [32]. A direct band gap semiconductor was assumed for these samples since a linear region just above the gap edges was observed with n = 2.

The linear part of the curve was extrapolated to $[F(R)\cdot h\nu]^2 = 0$ to estimate the direct band gap energy shown in Fig. 6. Inset of Fig. 6 shows that the values of the direct band gap (Eg) of the Co-doped ZnO samples decreases with increasing x. A similar decrease in the band gap energy with Co concentration has been reported in Co-doped ZnO thin films by Kim and Park [26], although an opposite behaviour was observed by Schwartz et al. [33] in $Zn_{1-x}Co_xO$ nanocrystals. Kim and Park [26] have argued that the band gap narrowing with increasing x is due to the sp–d exchange interactions between the band electrons and the localized d electrons of the substituted Co^{2+} ions. Ando et al. [34] reported that the magneto-optical effect in $Zn_{1-x}Co_xO$ is the largest observed between different TM dopants used indicating a strong exchange interaction between the electrons of the strip and sp of localized electrons, supporting this possibility.

Figure 7 shows the room temperature PL spectra under the excitation of 325 nm for all the samples. There are

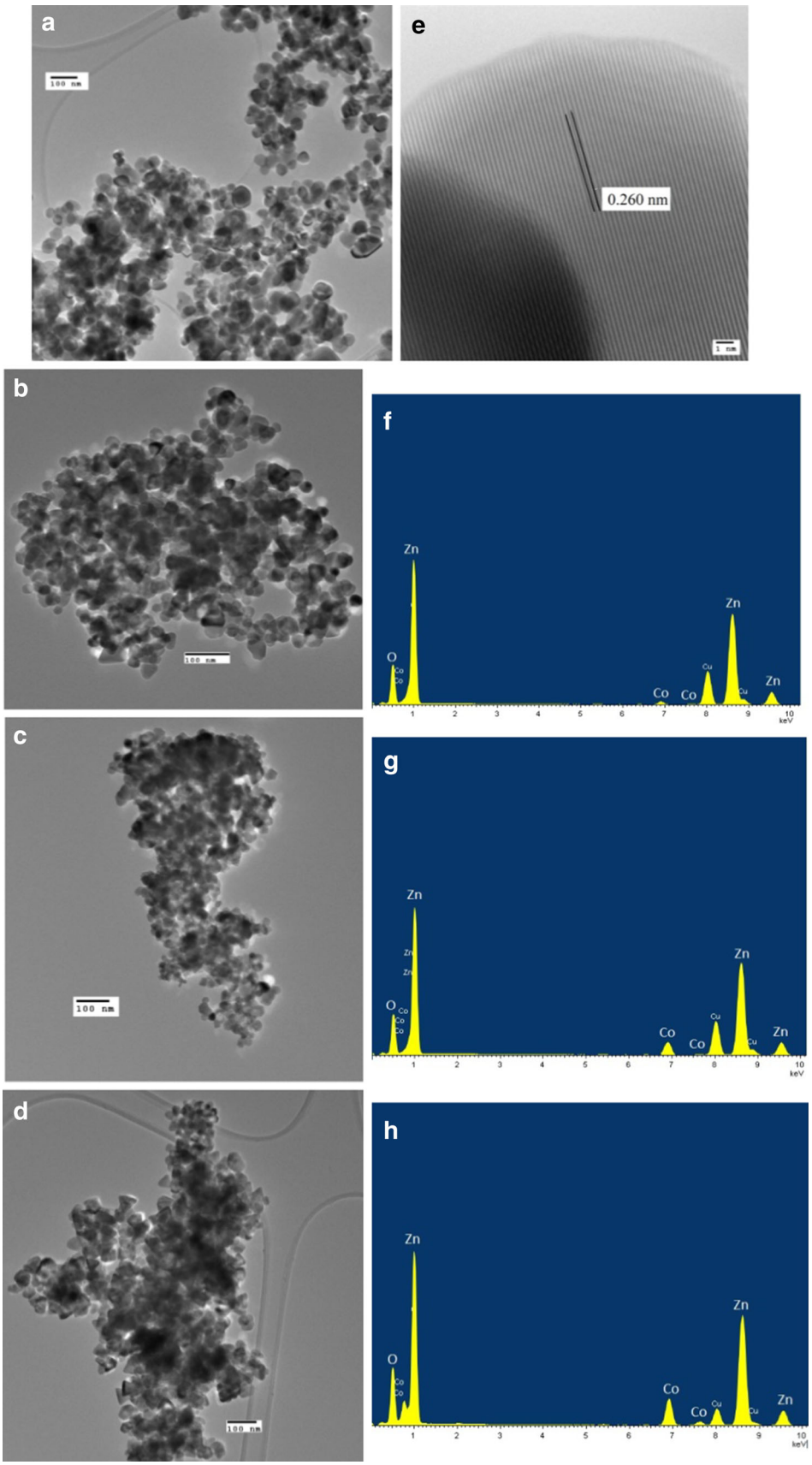

Fig. 4 HR-TEM images and EDX analysis of **a** ZnO, **b** $Zn_{0.99}Co_{0.01}O$, **c** $Zn_{0.97}Co_{0.03}O$, **d** $Zn_{0.95}Co_{0.05}O$ nanoparticles

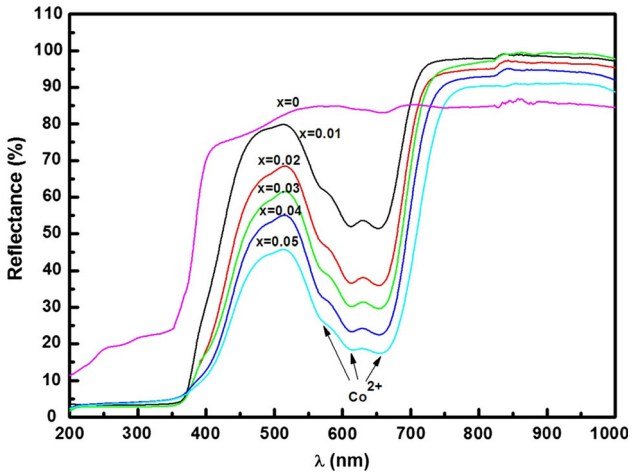

Fig. 5 Room-temperature diffuse reflectance spectra of $Zn_{1-x}Co_xO$ samples

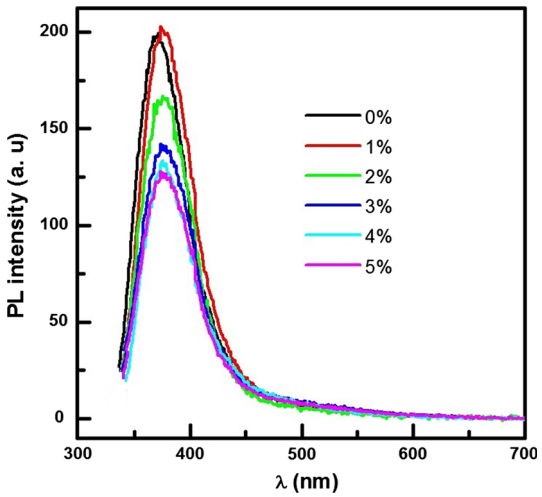

Fig. 7 Room-temperature PL spectra of the $Zn_{1-x}Co_xO$ nanoparticles

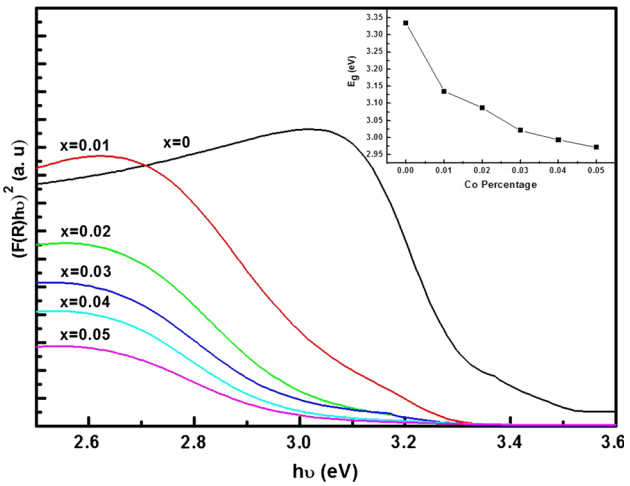

Fig. 6 Plot $[F(R)_*E]^2$ versus photon energy (hν). The *inset* showing the variation of the band gap energy with *x*

many works that report this type of study. These studies have shown the presence of UV Emission with different behaviors in adding Co. For example, some reports have revealed that Co-doped ZnO alloys show the red-shift of E_g for Co-doping [26] and Co- doped ZnO nanorods [35], while blue-shift phenomena have been also observed in Co-doped ZnO films [36] and epilayers [37]. The weak ultraviolet (UV) emission is assigned to the band-edge exciton of ZnO. Compared with the ZnO sample, the peak position of the UV emission shifts to short wavelength with increasing Co, which indicates that the band-gap of the ZnO nanowires can be adjusted by the doping of Co. It was suggested that the peak position of UV emission in Co doped ZnO nanowires is affected by Burstein–Moss effect and defects in the crystal. The peak shifts to short wavelength because of Burstein–Moss effect, while the defects in the crystals result in the emission peak shift to long wavelength. In our works, the peak positions for Co:ZnO samples slightly shift to the longer wavelength in comparison with the pure ZnO. This is due to the band gap narrowing of the ZnO nanocrystals with Co incorporation, as discussed in the previous section.

As the impurity effects dominate the PL from pure materials and the exciton moves through the materials, it encounters defects, and the exciton tends to decay in the vicinity of these centers. Under the same excitation condition, the intensity of the UV emission decreases with increasing Co, which suggests that the crystal quality is decreased by the doping of Co. As the diameter of the Co^{2+} irons is different from that of Zn^{2+}, more Co^{2+} irons substitute Zn^{2+}, more stress is induced in the materials, and the crystal quality is destroyed in some degree. Antony et al. [38] also found that the UV emission disappeared in the Co doped ZnO nanoclusters.

The magnetic properties of these powders were measured at room temperature (300 K). Figure 8 shows the dependence of magnetization with the applied magnetic field (M–H curves). For $Zn_{1-x}Co_xO$ (x = 0.01) sample, we observe a diamagnetic behaviour similar to that obtained in general for undoped ZnO. For increasing concentration (x = 0.03 and 0.05), magnetization curves show that the sample has both paramagnetic and ferromagnetic behavior. At lower field, we observed a weak ferromagnetic component and paramagnetic component at higher field values. The hysteresis loops for $Zn_{1-x}Co_xO$ (x = 0.03 and 0.05) samples shown in inset Fig. 8 present with the coercivity (Hc) values 117 and 43 Oe, respectively, and the remnant magnetization (Mr) values 3.52 10^{-4} and 1.510^{-4} emu/g. Regarding the origin of the ferromagnetic in our samples; there are several mechanisms that can induce ferromagnetism in general. For example, the

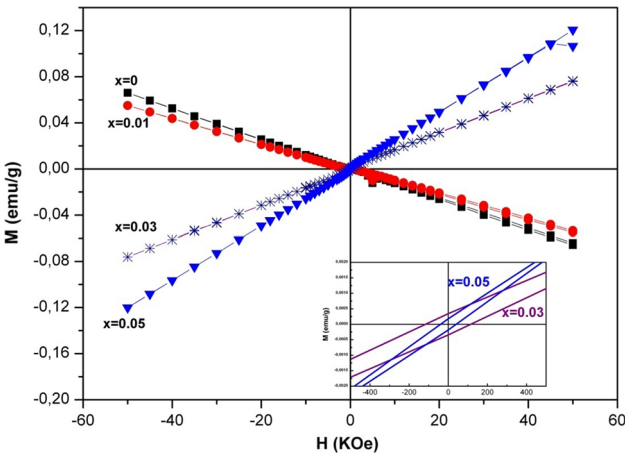

Fig. 8 Magnetization curve of $Zn_{1-x}Co_xO$ (x = 0.01, 0.03 and 0.05) at room temperature. *Inset* shows the magnified loop of $Zn_{1-x}Co_xO$ (x = 0.03 and 0.05)

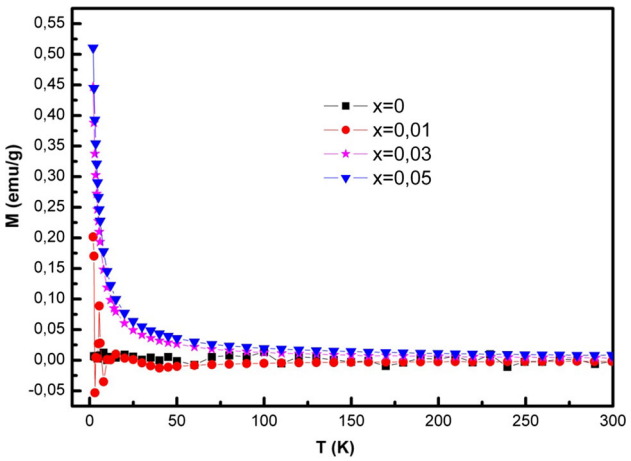

Fig. 9 Magnetization of of $Zn_{1-x}Co_xO$ (x = 0.01, 0.03 and 0.05) as a function of temperature

lattice defects and the secondary phases could be the origin of ferromagnetism ordering in this kind of systems. In our case, XRD shows that the lattice parameters increase with an increase of Co concentrations and that can affect the crystal quality. The presence of secondary phase of Co metal clusters has been ruled out by our XRD results. The ferromagnetism behavior could be also explained by the ferromagnetic coupling between substituting Co in the ZnO host [39]. Another mechanism related to the concept of bound magnetic polarons (BMPs) in connection with magnetic semiconductors can be introduced here to explain the origin of the ferromagnetism in our system [40, 41]. In the current experiment, the doping of Co impurity produced a number of oxygen vacancies and/or interstitial zinc that may act as shallow donor electrons and form BMPs. The overlapping of the polarons created a spin-split impurity band, which can mediate the Co–Co coupling in a ferromagnetism way, and thus, resulted in the ferromagnetic behavior of the sample. As Co dopant increased, it is more probable for the doped Co^{2+} cations to occupy the next nearest lattice sites. The nearest Co–Co pairs then coupled in an antiferromagnetic way [17] and suppressed the magnetization [42]. This interpretation can explained the decrease in Saturation for sample with x = 0.05 (3.52 10^{-4} emu/g compared to the value obtained for x = 0.03 (1.510^{-4} emu/g). We can conclude that the room temperature ferromagnetism in our samples could be related to the defects and/or the coupling between substituting Co in the ZnO host. Therefore, more studies have to be done to understand the room-temperature ferromagnetism in TM-doped ZnO.

Figure 9 shows the magnetization as a function of temperature (T). The temperature dependent behaviors are discussed based on a simple molecular field theory. First, the magnetization of the $Zn_{1-x}Co_xO$ (x = 0.01) sample shows a diamagnetic behavior. In addition, the magnetization of two other samples diverges as the temperature approaches zero, indicating that these samples contain a paramagnetic component dominating. These results are in good agreement with measurements (M–H).

4 Conclusion

Nanocrystalline $Zn_{1-x}Co_xO$ powders have been synthesized by a simple sol–gel method. The synthesis protocol is based on a slow hydrolysis of the precursor using an esterification reaction, followed by a supercritical drying in EtOH. XRD results indicated that all the synthesized undoped and Co-doped ZnO samples had the wurtzite structure and no secondary phases was detected which indicated that Co ions substituted for Zn ions. TEM results revealed that the prepared Co doped ZnO nanoparticles are nearly spherical in shape with particle size <30 nm, which is in good agreement with the size obtained from XRD. The band gap energy of the samples decreases from 3.33 (undoped ZnO) to 2.97 eV (5 mol% Co:ZnO), indicating that Co doping has a crucial influence on the energy band structure of ZnO. Furthermore, the $Zn_{1-x}Co_xO$ samples exhibit diamagnetic characteristics for x = 0.01 and weak ferromagnetic with more doping content of Co^{2+}, the ferromagnetic behavior is suppressed and paramagnetic nature is observed at higher field values.

References

1. A.P. Alivisatos, Science **271**, 933–937 (1996)
2. D.J. Norris, N. Yao, F.T. Charnock, T.A. Kennedy, Nano Lett. **1**, 429–433 (2001)
3. M. Nirmal, L. Brus, Acc. Chem. Res. **32**, 407–414 (1999)

4. H.M. Yang, S. Nie, Mater. Chem. Phys. **114**, 279–282 (2009)
5. M. Yang, Z.X. Guo, K.H. Qiu, J.P. Long, G.F. Yin, D.G. Guan, S.T. Liu, S.J. Zhou, Appl. Surf. Sci. **256**, 4201–4205 (2010)
6. S.S. Lin, J.H. Song, Y.F. Lu, Z.L. Wang, Nanotechnology **20**, 365703 (2009)
7. M. Krunks, A. Katerski, T. Dedova, I.O. Acik, A. Mere, Sol. Energy Mater. Sol. Cells **92**, 1016–1019 (2008)
8. S. Rasouli, S.J. Moeen, J. Alloys Compd. **509**, 1915–1919 (2011)
9. J.B. Cui, Y.C. Soo, T.P. Chen, J. Phys. Chem. C **112**, 4475–4479 (2008)
10. Z. Sofer, D. Sedmidubský, S. Huber, J. Hejtmanek, M. Marysko, K. Jurek, M. Mikulics, J. Cryst. Growth **314**, 123–128 (2011)
11. X.R. Qu, D.C. Jia, Mater. Lett. **63**, 412–414 (2009)
12. Q. Chen, J.L. Wang, Chem. Phys. Lett. **474**, 336–341 (2009)
13. H.B. Carvalho, M.P.F. Godoy, R.W.D. Paes, M. Mir, A.O. Zevallos, F. Iikawa, M.J.S.P. Brasil, V.A. Chitta, W.B. Ferraz, M.A. Boselli, A.C.S. Sabioni, J. Appl. Phys. **108**, 033914 (2010)
14. F. Ochanda, K. Cho, D. Andala, T.C. Keane, A. Atkinson, W.E. Jones, Langmuir **25**, 7547–7552 (2009)
15. B.Q. Wang, X.D. Shan, Q. Fu, J. Iqbal, Y. Lv, H.G. Fu, D.P. Yu, Phys. E **41**, 413–417 (2009)
16. N. Bahadur, A.K. Srivastava, S. Kumar, M. Deepa, B. Nag, Thin Solid Films **518**, 5257–5264 (2010)
17. P.K. Sharma, R.K. Dutta, A.C. Pandey, J. Colloid Interface Sci. **345**, 149–153 (2010)
18. X.Y. Xu, C.B. Cao, J. Alloys Compd. **501**, 265–268 (2010)
19. J.H. Yang, L.Y. Zhao, X. Ding, L.L. Yang, Y.J. Zhang, Y.X. Wang, H.L. Liu, Mater. Sci. Eng. B **162**, 143–146 (2009)
20. M.E. Mercurio, A.W. Carbonari, M.R. Cordeiro, R.N. Saxena, L.Z. D'Agostino, J. Magn. Magn. Mater. **322**, 1195–1197 (2010)
21. X.L. Zhang, R. Qiao, J.C. Kim, Y.S. Kang, Cryst. Growth Des. **8**, 2609–2613 (2008)
22. A. Singhal, S.N. Achary, J. Manjanna, S. Chatterjee, P. Ayyub, A.K. Tyagi, J. Phys. Chem. C **114**, 3422–3430 (2010)
23. J. El Ghoul, C. Barthou, L. El Mir, Superlattices Microstruct. **51**, 942–951 (2012)
24. L.W. Yang, X.L. Wu, T. Qiu, G.G. Siu, P.K. Chu, J. Appl. Phys. **99**, 074303-1–074303-5 (2006)
25. J. El Ghoul, C. Barthou, L. El Mir, Phys. E Low dimens. Syst. Nanostruct. **44**, 1910–1915 (2012)
26. K.J. Kim, Y.R. Park, Appl. Phys. Lett. **81**, 1420–1422 (2002)
27. Ping Li, Sha Wang, Jibiao Li, YuWei. J. Lumin. **132**, 220–225 (2012)
28. S. Deka, P.A. Joy, Solid State Commun. **134**, 665–669 (2005)
29. D.K. Sardar, J.B. Gruber, B. Zandi, M. Ferry, M.R. Kokta, J. Appl. Phys. **91**, 4846–4852 (2002)
30. S. Ramachandran, A. Tiwari, J. Narayan, Appl. Phys. Lett. **84**, 5255–5257 (2004)
31. A. Fouchet, W. Prellier, P. Padhan, Ch. Simon, B. Mercey, V.N. Kulkarni, T. Venkatesan, J. Appl. Phys. **95**, 7187–7189 (2004)
32. A.T. Kuvarega, R.W.M. Krause, B.B. Mamba, J. Phys. Chem. C **115**, 22110–22120 (2011)
33. D.A. Schwartz, N.S. Norberg, Q.P. Nguyen, J.M. Parker, D.R. Gamelin, J. Am. Chem. Soc. **125**, 13205–13218 (2003)
34. K. Ando, H. Saito, Z. Jin, T. Fukumura, M. Kawasaki, Y. Matsumoto, H. Koinuma, J. Appl. Phys. **89**, 7284–7286 (2001)
35. Y.J. Li, C.Y. Wang, M.Y. Lu, K.M. Li, L.J. Chen, Cryst. Growth Des. **8**, 2598–2602 (2008)
36. J.H. Kim, H. Kim, D. Kim, S.G. Yoon, W.K. Choo, Solid State Commun. **131**, 677–680 (2004)
37. W. Pacuski, D. Ferrand, J. Cibert, C. Deparis, J.A. Gaj, P. Kossacki, C. Morhain, Phys. Rev. B **73**, 035214–035226 (2006)
38. J. Antony, S. Pendyala, A. Sharma, X.B. Chen, J. Morrison, L. Bergman, Y. Qiang, J. Appl. Phys. **97**, 10D307 (2005)
39. S. Yang, Y. Zhang, J. Magn. Magn. Mater. **334**, 52–58 (2013)
40. R. Janisch, P. Gopal, N.A. Spaldin, J. Phys. Condens. Matter **17**, R657–R689 (2005)
41. J.M.D. Coey, M. Venkatesan, C.B. Fitzgerald, Nat. Mater. **4**, 173–179 (2005)
42. T. Büsgen, M. Hilgendorff, S. Irsen, F. Wilhelm, A. Rogalev, D. Goll, M. Giersig, J. Phys. Chem. C **112**, 2412–2417 (2008)